

Article

Pt-Chitosan-TiO₂ for Efficient Photocatalytic Hydrogen Evolution via Ligand-to-Metal Charge Transfer Mechanism under Visible Light

 Yanru Liu ¹, Jingyun Mao ² , Yiwei Huang ¹, Qingrong Qian ² , Yongjin Luo ², Hun Xue ^{2,*} and Songwei Yang ^{2,*}
¹ College of Life Sciences, Fujian Normal University, Fuzhou 350117, China; yrliu@fjnu.edu.cn (Y.L.); hywadgjmtw@163.com (Y.H.)

² College of Environmental Science and Engineering, Fujian Normal University, Fujian Key Laboratory of Pollution Control & Resource Reuse, Fuzhou 350007, China; mjy19960427@163.com (J.M.); qrqian@fjnu.edu.cn (Q.Q.); yongjinluo@fjnu.edu.cn (Y.L.)

* Correspondence: xuehun@fjnu.edu.cn (H.X.); hxxacl@163.com (S.Y.)

Abstract: The Pt-chitosan-TiO₂ charge transfer (CT) complex was synthesized via the sol-gel and impregnation method. The synthesized photocatalysts were thoroughly characterized, and their photocatalytic activity were evaluated toward H₂ production through water reduction under visible-light irradiation. The effect of the preparation conditions of the photocatalysts (the degree of deacetylation of chitosan, addition amount of chitosan, and calcination temperature) on the photocatalytic activity was discussed. The optimal Pt-10%DD75-T200 showed a H₂ generation rate of 280.4 μmol within 3 h. The remarkable visible-light photocatalytic activity of Pt-chitosan-TiO₂ was due to the CT complex formation between chitosan and TiO₂, which extended the visible-light absorption and induced the ligand-to-metal charge transfer (LMCT). The photocatalytic mechanism of Pt-chitosan-TiO₂ was also investigated. This paper outlines a new and facile pathway for designing novel visible-light-driven photocatalysts that are based on TiO₂ modified by polysaccharide biomass wastes that are widely found in nature.

Keywords: photocatalyst; TiO₂; chitosan; H₂ evolution; LMCT; visible light



Citation: Liu, Y.; Mao, J.; Huang, Y.; Qian, Q.; Luo, Y.; Xue, H.; Yang, S. Pt-Chitosan-TiO₂ for Efficient Photocatalytic Hydrogen Evolution via Ligand-to-Metal Charge Transfer Mechanism under Visible Light. *Molecules* **2022**, *27*, 4673. <https://doi.org/10.3390/molecules27154673>

Academic Editors: Imre Miklós Szilágyi, Omid Mahian, Klára Hernádi and Ottó Horváth

Received: 20 May 2022

Accepted: 19 July 2022

Published: 22 July 2022

Publisher's Note: MDPI stays neutral with regard to jurisdictional claims in published maps and institutional affiliations.



Copyright: © 2022 by the authors. Licensee MDPI, Basel, Switzerland. This article is an open access article distributed under the terms and conditions of the Creative Commons Attribution (CC BY) license (<https://creativecommons.org/licenses/by/4.0/>).

1. Introduction

In recent years, semiconductor photocatalysis driven by solar light has had broad application prospects in the field of environmental chemistry [1–4]. As a photocatalyst for environmental purification and solar energy conversion, titanium dioxide (TiO₂) is known for its high oxidation power, low price, chemical stability, and non-toxicity [5–7]. However, pure TiO₂, with a band gap of 3.2 eV, can only be excited by ultraviolet light (<5% of solar energy), which limits its practical applications [8,9]. Therefore, many studies have been conducted to obtain visible-light-responsive TiO₂-based photocatalysts, including dye sensitization [10,11], impurity doping [12–14], coupling with other semiconductors [15–17], etc.

Another method of visible-light activation of TiO₂ is the formation of charge transfer (CT) complexes between TiO₂ and organic molecules that do not absorb visible light by themselves [18]. The CT complexes generate visible-light-driven ligand-to-metal charge transfer (LMCT) that represents the transfer of the electrons from the highest occupied molecular orbital (HOMO) of adsorbates to the conduction band (CB) of TiO₂, which changes its optoelectronic properties [19]. Up to now, organic molecules such as ethylene diamine tetraacetic acid (EDTA) [20], phenol [21], catechol [22], dopamine [23], and glucose [24] have been reported as surface ligands for the modification of TiO₂ to extend its spectrum response range into the visible-light region. For instance, EDTA-TiO₂, a typical LMCT complex, induces a visible-light absorption of 550 nm and can be applied to reduce Cr(VI) to Cr(III) under visible-light irradiation, which can be attributed to the LMCT mechanism, where the visible-light irradiation directly excites electrons from the HOMO of EDTA

to the conduction band (CB) of TiO₂ [25]. Kim et al. reported that glucose absorbed on the surface of TiO₂ nanoparticles can easily form complexes with TiO₂ via their hydroxyl groups. Glucose-TiO₂ complexes showed photocatalytic activities for the reduction of Cr(VI) to Cr(III) and O₂ to H₂O₂ under visible-light irradiation, although neither glucose nor TiO₂ can absorb visible light [26]. Li et al. demonstrated that the hydroxyl groups on a cellulose nanocrystal (CNC) can guide the growth of TiO₂ nanoparticles on it and induce the formation of CT complexes. TiO₂/CNC nanocomposites show an excellent performance for photoreduction of Cr(VI) under visible light [27]. Chitosan, derived from the partial deacetylation of chitin that is extracted from the shell of marine crustaceans, possesses functional groups such as the amino group and hydroxyl group [28]. The degree of deacetylation of chitosan signifies the proportion of free amino groups in chitosan. The higher the degree of deacetylation and the larger the quantity of acetyl groups removed from acetyl amino groups, the more obvious the chemical properties of the amino groups. Chitosan, being rich in natural resources and low in cost, has been widely applied in the photocatalytic field and absorbing heavy metal ions [29,30]. Li et al. fabricated chitosan/g-C₃N₄/TiO₂ nanofibers for Cr(VI) removal through adsorption and photocatalytic processes [30]. Balakrishnan et al. immobilized TiO₂ on chitosan to achieve the recyclable photocatalyst that exhibits an excellent 2,4-dichlorophenoxyacetic acid performance under UV light [31]. However, chitosan and TiO₂ complex for H₂ evolution under visible-light irradiation by a LMCT mechanism has not been reported.

In this study, Pt-chitosan-TiO₂ LMCT complexes were prepared and employed as photocatalysts for H₂ production under visible-light irradiation. Synthetic conditions were optimized to achieve the highest photocatalytic activity, including the optimization of different degrees of deacetylation of chitosan, temperature of preparation, and the amount of chitosan. The as-obtained Pt-chitosan-TiO₂ LMCT complexes achieved a high H₂ evolution rate of 280.4 μmol within 3 h under visible-light irradiation. Furthermore, we present the photocatalytic mechanism of Pt-chitosan-TiO₂ LMCT complexes.

2. Results and Discussion

2.1. Physicochemical Properties of the Obtained Samples

The reaction process of the deacetylation of chitin is shown in Figure 1a. Chitosan was obtained by removing some or all of the acetyl groups from chitin after high-temperature treatment with concentrated alkali. Figure 1b shows that the deacetylation degree of chitosan varied with the reaction time. The change in deacetylation degree presented a rapidly increasing trend within 60 min. The trend slowly increased after 60 min, which we attributed to the increasing number of acetyl groups in the solution during the reaction process. Figure 1c presents the TGA curve of the chitosan. There are two stages on the curve of the chitosan from 30 to 800 °C. A weight loss of about 3.8% between 30 and 100 °C was due to the loss of water molecules in chitosan. The enormous weight loss of 94.2% between 230 and 570 °C was ascribed to the decomposition of the organic component in chitosan [32]. The results indicated that the chitosan can remain unchanged when the temperature is below 230 °C.

The XRD patterns of DD45 and DD75 are depicted in Figure 1d. The broad peaks at 20.5° were attributed to (110) the plane of chitosan [30]. The intensity of the diffraction peaks decreased with the increase in the degree of deacetylation, which is in accordance with the literature [33]. The XRD patterns of Pt-10%DD75-T200, Pt-10%DD45-T200, and Pt-T200 are shown in Figure 1e. All of the samples exhibited diffraction peaks corresponding to standard anatase TiO₂ (JCPDS No.01-073-1764) [34]. A diffraction peak at 19.9° was indexed to chitosan in Pt-10%DD45-T200. However, the peak attributed to chitosan disappeared in the XRD pattern of Pt-10%DD75-T200, which was due to the complete dissolution of DD75 in TiO₂ sol. Compared with DD45, DD75 had better solubility in TiO₂ sol, which is more conducive for forming CT complexes with TiO₂. Furthermore, the average crystal diameters of Pt-T200, Pt-10%DD45-T200, and Pt-10%DD75-T200 were calculated from the Scherrer equation, based on the half-width of the strongest diffraction peak of anatase

TiO₂. The results are 6.00, 5.45, and 5.42 nm, which demonstrated that the degrees of deacetylation have little effect on the microstructure of TiO₂.

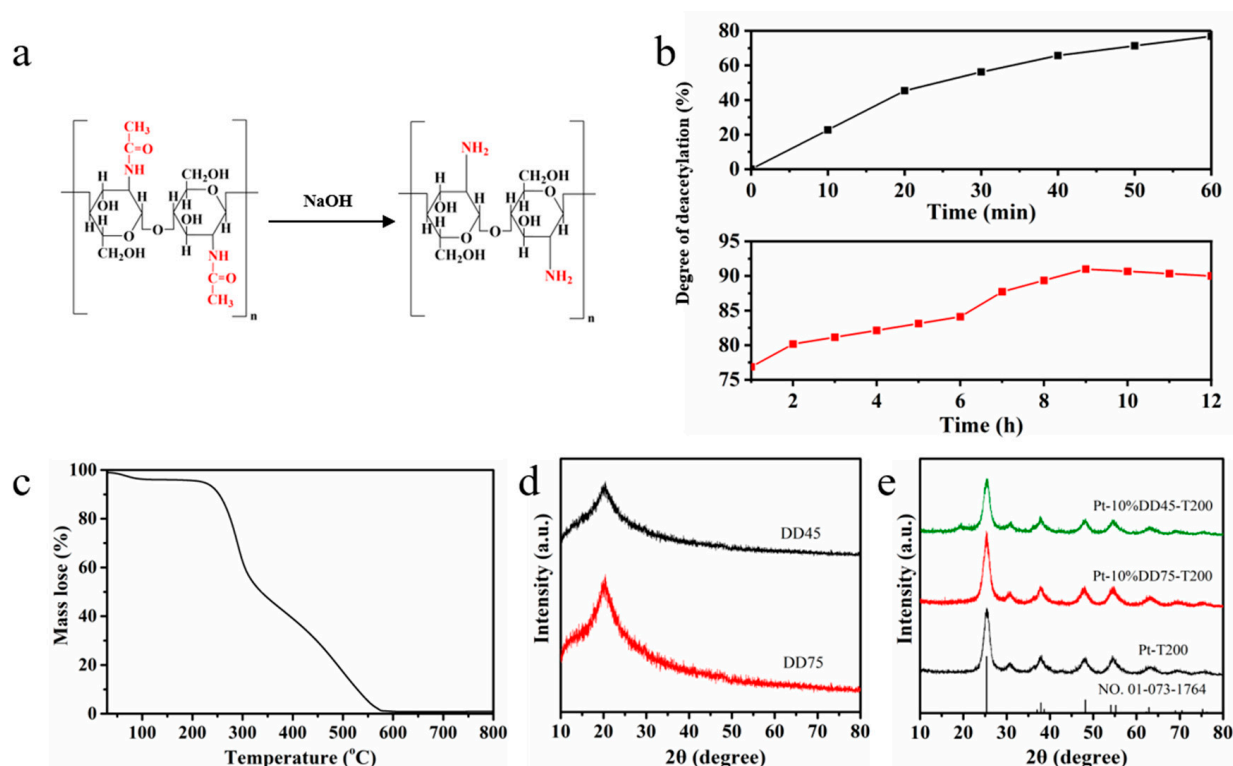


Figure 1. (a) Graph of degree of deacetylation of chitosan varying with the reaction time; (b) reaction of the deacetylation of chitin; (c) TGA curve of chitosan; (d) XRD patterns of DD45 and DD75, and (e) XRD patterns of Pt-T200, Pt-10%DD45-T200, and Pt-10%DD75-T200.

The UV–vis diffuse reflectance spectra of DD45, DD75, Pt-T200, and the as-prepared Pt-chitosan-TiO₂ samples are displayed in Figure S1a–c and Figure 2a. As can be seen, the Pt-T200, DD45, and DD75 samples showed no visible-light absorption, and Pt-T200 only showed an absorption edge at about 393 nm, indicating that it can only be excited by UV light. On the other hand, Pt-chitosan-TiO₂ CT complexes extended the absorption from the UV region to the visible-light region. In addition, the absorption edges of Pt-DD45-T200 and Pt-DD75-T200 were 558 and 778 nm, respectively. Such a shift was attributed to the formation of the LMCT complex between chitosan and TiO₂.

The enhanced visible absorption was attributed to the formation of the CT complex, which may increase the photocatalytic activity under visible-light irradiation [27].

The FT-IR spectra of the chitosan, Pt-10%DD45-T200, Pt-10%DD75-T200, and Pt-T200 are shown in Figure 2b. In the FT-IR spectrum of Pt-T200, the stretching and bending of O–H near 3370 cm⁻¹ was observed [8]. The peak at 1383 cm⁻¹ was assigned to the –CH₂ and –CH₃ (due to the incomplete hydrolysis of tetrabutyl titanate), and the peaks from 400 to 800 cm⁻¹ related to the typical vibration of the O–Ti–O bonding of the TiO₂ structure [34]. With respect to chitosan, the peak at 3415 cm⁻¹ was attributed to the stretching vibration of both O–H and –NH₂; the peaks located around 1655 and 1599 cm⁻¹ were attributed to the amide I group and –NH deformation, respectively. The peak at 1422 cm⁻¹ was due to the bending vibration of –NH₂ [35]. As for Pt-10%DD45-T200 and Pt-10%DD75-T200, the peaks located at 1404 cm⁻¹ were assigned to the –CH₂, –CH₃, and the bending vibration of –NH₂. All the main characteristic peaks of TiO₂ and the bending vibration of –NH₂ appeared in the FT-IR spectra of Pt-10%DD75-T200 and Pt-10%DD45-T200, indicating that the chitosan and TiO₂ composites were successfully synthesized.

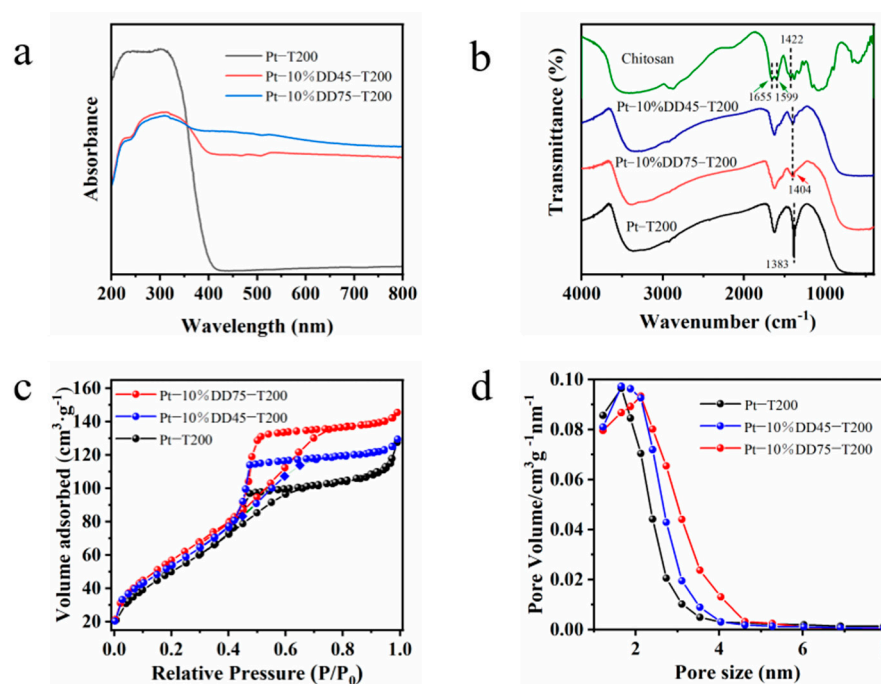


Figure 2. (a) UV-vis diffuse reflectance spectra, (b) FT-IR spectra, (c) N_2 adsorption-desorption isotherms, and (d) BJH pore size distribution of as-prepare Pt-Chitosan-TiO₂ samples.

The N_2 adsorption-desorption isotherms (Figure 2c) show that all three samples (Pt-10%DD75-T200, Pt-10%DD45-T200, and Pt-T200) displayed type-IV isotherms, which is a typical adsorption behavior of mesoporous materials. Furthermore, Pt-10%DD75-T200 ($221.9 \text{ m}^2/\text{g}^1$) showed a higher specific surface area than that of Pt-10%DD45-T200 ($208.6 \text{ m}^2/\text{g}^1$) and Pt-T200 ($198.4 \text{ m}^2/\text{g}^1$). The average pore sizes of Pt-10%DD75-T200, Pt-10%DD45-T200, and Pt-T200 are about 4.1, 3.8, and 4.0 nm (Figure 2d), respectively. This increased specific surface area can increase the contact area between reactants and photocatalysts, leading to higher photocatalytic activity.

The SEM images of DD75 and DD45 are shown in Figure 3a,b. Both of them were composed of particles with homogeneous, compact, and wrinkled surfaces. In addition, the interface between DD45 particles was more distinct than that between DD75 particles. As shown in Figure 3c, the SEM image of Pt-T200 depicts that it entirely consisted of nanoparticles. As shown in Figure 3d,e, the SEM images of Pt-DD75-T200 and Pt-DD45-T200 both reveal a uniform nanoparticle morphology similar to that of TiO₂. However, the aggregation phenomenon of Pt-DD75-T200 nanoparticles was less than that of Pt-T200 and Pt-DD45-T200, suggesting that the addition of DD75 contributed to the dispersion of TiO₂ nanoparticles.

Figure 4a–c present the TEM images of TiO₂, Pt-10%DD45-T200, and Pt-10%DD75-T200, respectively. As can be seen, all of the samples consisted of nanoparticles. Moreover, the nanoparticles of Pt-10%DD75-T200 were more uniformly distributed than that of Pt-10%DD45-T200 and Pt-T200, which is in good agreement with the result of the SEM images. Clear diffraction patterns with interdistance $d = 0.35 \text{ nm}$ and $d = 0.19 \text{ nm}$ can be observed in the HRTEM image of Pt-10%DD75-T200 in Figure 4d, assigned to the (101) and (200) crystal planes of TiO₂, respectively [34]. The average particle size values of Pt-T200, Pt-10%DD75-T200, and Pt-10%DD45-T200 nanoparticles were about 6 nm, indicating that the particle size of TiO₂ was unchanged with the existence of chitosan and Pt. Furthermore, the EDS mapping analysis of Pt-10%DD75-T200 (Figure 4e–k) shows a coexistence and homogeneous dispersion of Ti, O, C, N, and Pt atoms in the nanoparticles, demonstrating the successful composition of TiO₂ and chitosan, as well as the loading of Pt.

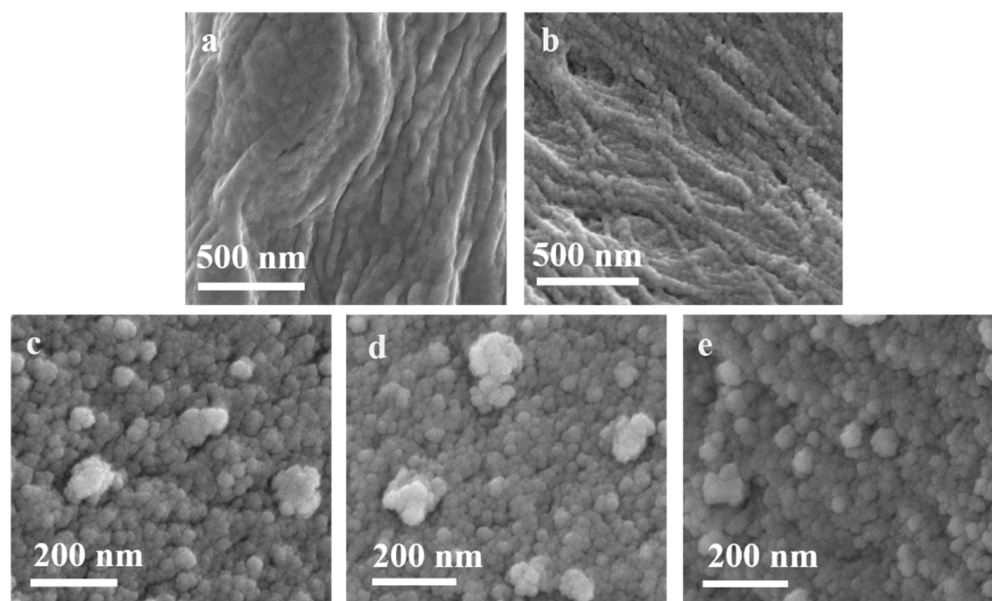


Figure 3. SEM images of (a) DD45, (b) DD75, (c) Pt-T200, (d) Pt-10%DD45-T200, and (e) Pt-10%DD75-T200.

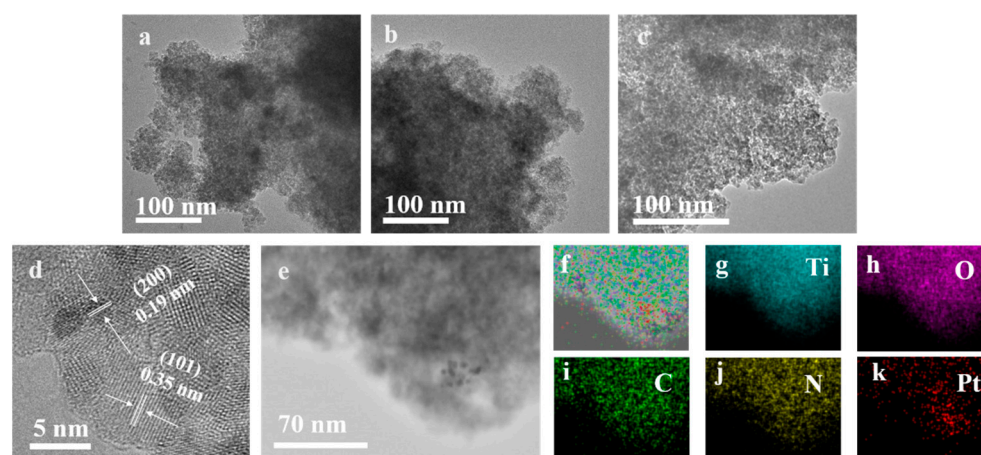


Figure 4. TEM images of (a) Pt-T200, (b) Pt-10%DD45-T200, and (c) Pt-10%DD75-T200; HRTEM image of (d) Pt-10%DD75-T200; (e–k) EDS elemental mapping images of Pt-10%DD75-T200.

XPS analysis was employed to determine the specific bonding and chemical states of elements in Pt-T200 and Pt-10%DD75-T200 photocatalysts. As shown in Figure 5a, the wide-scan XPS spectrum of Pt-T200 illustrated the presence of Ti, O, C, and Pt elements; that of Pt-10%DD75-T200 illustrated the presence of Ti, O, N, C, and Pt elements. As shown in Figure 5b, the peaks located at 458.4 and 464.1 eV corresponded to Ti 2p_{3/2} and Ti 2p_{1/2}, respectively, suggesting that the oxidation state of Ti was +4 [36]. As displayed in Figure 5c, the peaks located at 529.6 and 530.4 eV belonged to the lattice oxygen (Ti–O) and adsorbed oxygen (Ti–OH), respectively [8]. In Figure 5d, the N 1s peaks located at 399.8 eV were assigned to the N element contained in –NH₂/–NH and –NH₃⁺ groups in chitosan [36], while the peaks located at 401.3 eV originated from surface adsorbed or contaminated nitrogen species. The C 1s spectrum in Figure 5e displays the peaks located at 284.8, 286.4, and 288.7 eV, corresponding to the C signal in C–C/C=C bonds, C–OH and C=O, respectively [37]. The C1s signal for Pt-T200 was ascribed to the adsorbed carbon contaminants from the ambience, while the signal for Pt-10%DD75-T200 was due to the carbonaceous materials in chitosan. The Pt 4f high-resolution XPS spectrum shown in Figure 5f reveals two peaks at 70.5 and 74.2 eV, which were attributed to the Pt 4f_{7/2} and Pt 4f_{5/2} of Pt (0), respectively [38].

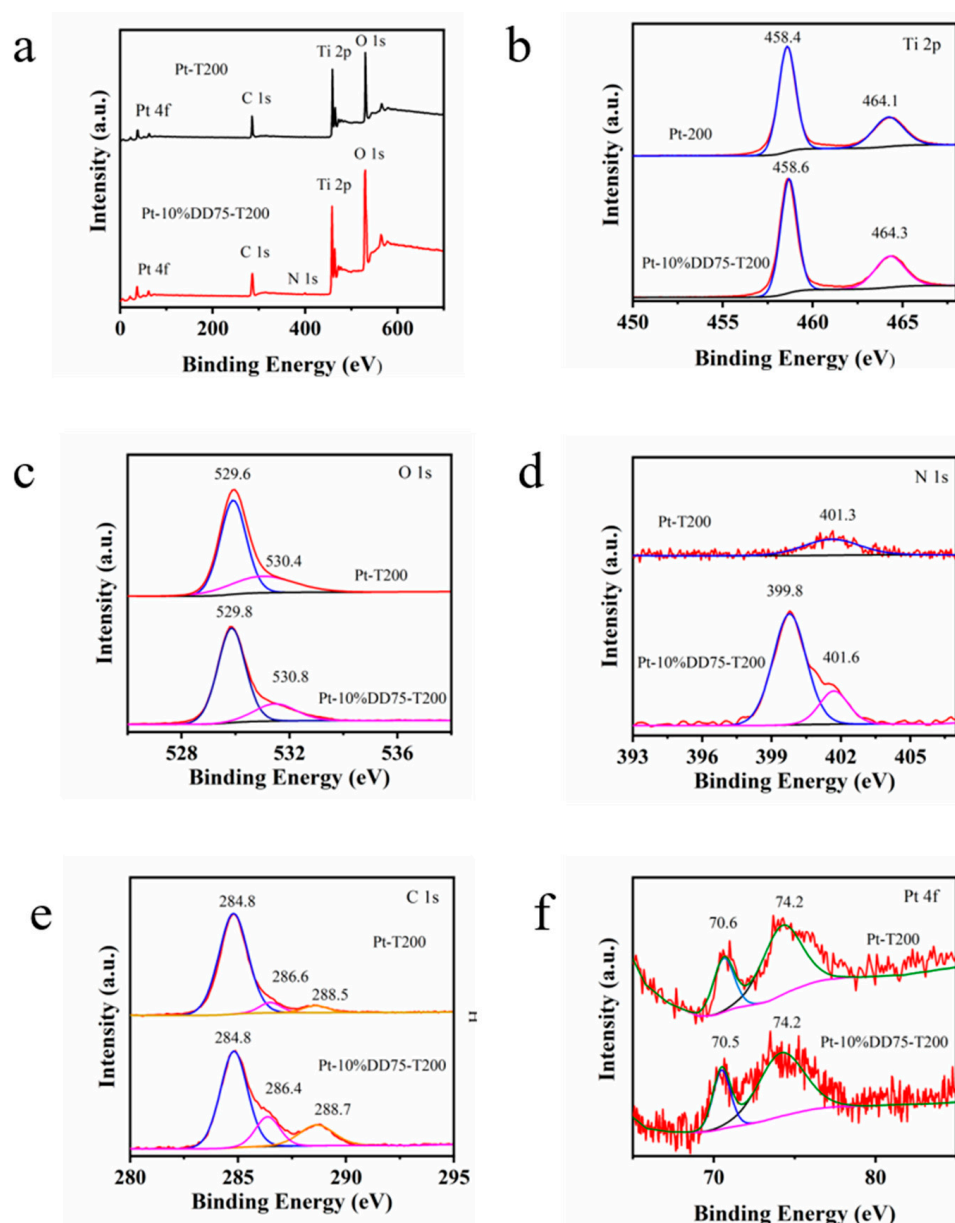


Figure 5. XPS spectra of Pt-10%DD75-T200: (a) survey, (b) Ti 2p, (c) O 1s, (d) N 1s, (e) C 1s, and (f) Pt 4f.

2.2. Photocatalytic H₂ Evolution Performance

The photocatalytic performance of the as-prepared samples was evaluated by water-splitting for H₂ production under visible light, and the results are shown in Figure 6a–c. Very little H₂ was detected over Pt-T200 (2.7 μmol) under visible-light irradiation as a result of its large band gap. A significant increase in photocatalytic activity was seen after the addition of chitosan. The evolution rates of H₂ after 3 h of visible-light illumination for Pt-10%DDn-T200 (*n* = 25, 45, 65, 75, 85 and 95) were 36.2, 72.8, 270.1, 280.4, 270.4, and 257.1 μmol, respectively. The higher photocatalytic activity of Pt-10%DDn-T200 (*n* = 65, 75, 85 and 95) compared with that of Pt-10%DDn-T200 (*n* = 25 and 45) may have been due to the solubility of DDn in titanium sol being improved with the increase in the degree of deacetylation. This facilitated the condensation of the hydroxyl groups in both chitosan and TiO₂ and aided the formation of the CT complex in the process of calcination, leading to the outstanding visible-light activity. Furthermore, the formation of CT complexes between TiO₂ and chitosan could absorb visible-light through the LMCT mechanism, leading to the outstanding visible-light activity. When the deacetylation degree of chitosan reached 75%, Pt-10%DD75-T200 showed an optimal photocatalytic activity for water reduction. The

effects of calcination temperature and the amount of chitosan on the photocatalytic activity of Pt-mDD75-Tt ($m = 5\%$, 10% , and 20%) were investigated. After 3 h of visible-light illumination, the evolution rates of H_2 for Pt-10%DD75-Tt ($t = 150, 200$ and $250\text{ }^\circ\text{C}$) were $217.7, 280.4,$ and $198.3\text{ }\mu\text{mol}$, respectively. The lower photocatalytic activity of the sample calcinated at $150\text{ }^\circ\text{C}$ could have been due to an incomplete conversion from titanium hydroxide to TiO_2 and a lower crystallinity of TiO_2 . A calcination temperature of $250\text{ }^\circ\text{C}$ led to the partial decomposition of chitosan and, consequently, the weak photocatalytic activity. The performance of Pt-10%DD75-T200 was also much higher than that of Pt-5%DD75-T200 ($167.7\text{ }\mu\text{mol}^1$) and Pt-15%DD75-T200 ($248.3\text{ }\mu\text{mol}$). The photocatalytic activity improved with increasing amounts of chitosan due to increasing amounts of CT complexes. When the amount of chitosan was further increased, the photocatalytic activity decreased. This may have been due to excess chitosan occupying the photocatalytically active sites of TiO_2 . Control experiments for photocatalytic H_2 evolution reaction over Pt-10%DD75-T200 are shown in Figure S2. The figure demonstrates that no H_2 could be detected in the absence of TEOA, irradiation and a photocatalyst. Figure S3 presents the action spectra of Pt-10%DD75-T200. As can be seen, the apparent quantum efficiencies at the different illumination wavelengths of Pt-10%DD75-T200 were in good accordance with the absorbance spectrum. Furthermore, the FT-IR and XPS spectra of Pt-10%DD75-T200 before and after irradiation are shown in Figures S4 and S5, which indicated that the photocatalyst barely changed and confirmed its stability.

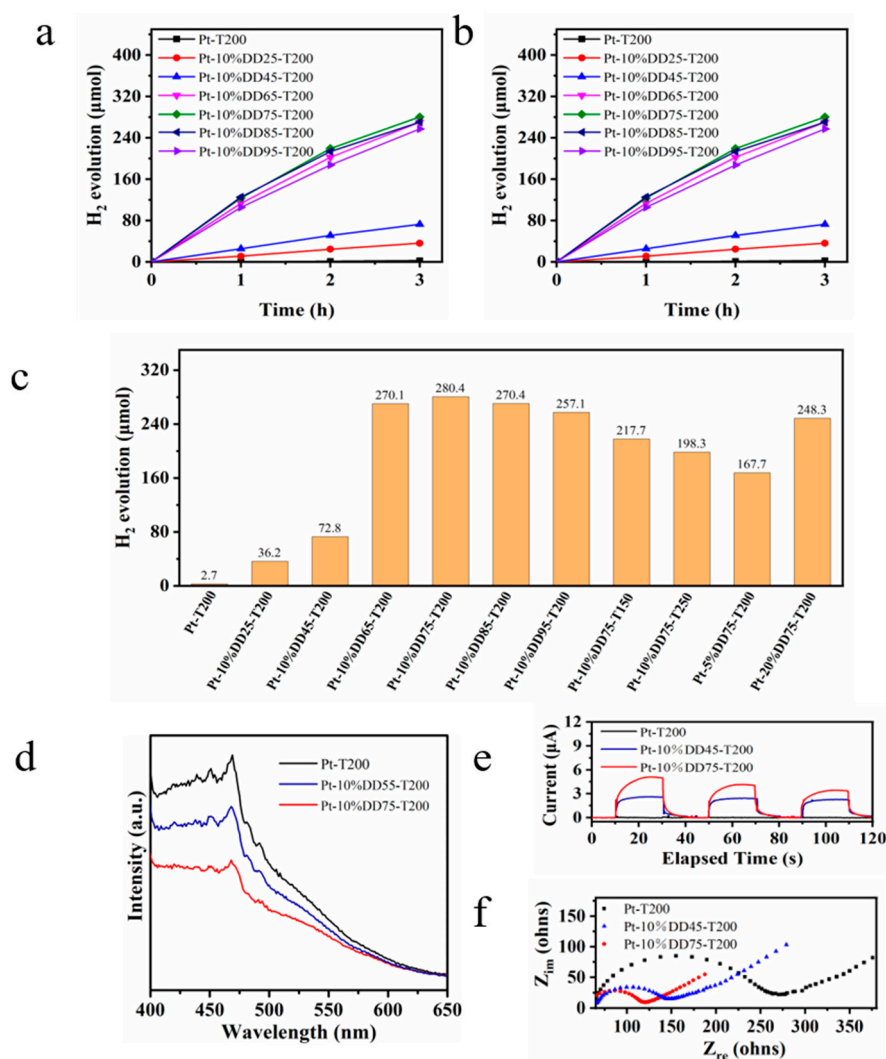


Figure 6. (a,b) Photocatalytic H_2 evolution, (c) H_2 evolution rates of as-prepared Pt-chitosan- TiO_2 samples ($\lambda > 420\text{ nm}$, $10\text{ vol}\%$ TEOA, $\text{pH} = 11.3$, 278 K), (d) emission spectra, (e) transient photocurrent

(0.1M Na₂SO₄, Ag/AgCl electrode, Pt plate, sample electrodes, pH = 11.3, 0 V), (f) EIS Nyquist plots of Pt-T200, Pt-10%DD45-T200, and Pt-10%DD75-T200 (0.1M KCl, Ag/AgCl electrode, Pt plate, sample electrodes, pH = 11.3, 0.2 V).

Photoluminescence spectroscopy was applied to study the migration, transfer, and recombination of electron-hole pairs generated by the photocatalyst. The excitation spectra for Pt-T200, Pt-10%DD45-T200, and Pt-10%DD75-T200 is shown in Figure S6 with the emission wavelength at 350 nm, which exhibited excitation peaks appearing at 358 nm. As presented in Figure 6d, the emission intensity followed the order of Pt-10%DD75-T200 < Pt-10%DD45-T200 < Pt-T200, which was opposite to the order of photocatalytic activity. The lower PL intensity was related to the slower recombination rate of electron-hole pairs. The photocurrent response curves and EIS Nyquist plots of Pt-T200, Pt-10%DD45-T200, and Pt-10%DD75-T200 are shown in Figure 6e,f. As can be seen, Pt-10%DD75-T200 showed the strongest photocurrent density and smallest semi-circle, indicating the highest photo-induced charge transfer and separation efficiency. In conclusion, these commendable photo- and electro-chemical characterizations support that the combination of chitosan and TiO₂ leads to efficient interfacial charge transfer and the suppression of photoexcited charge recombination.

2.3. Mechanism of Photocatalytic Reaction

Based on the above analysis and experimental results, a possible photocatalytic mechanism for water reduction over Pt-chitosan-TiO₂ CT complex photocatalyst was proposed (Figure 7). In this process, chitosan attaches to the TiO₂ surface through their hydroxyl groups, sensitizing the TiO₂ by forming LMCT complexes. Typically, electrons can be easily excited from the HOMO level of chitosan and transferred to the CB of TiO₂ under visible-light irradiation. In addition, due to a higher work function of Pt (5.65 eV), electrons are transferred to the Pt cocatalyst and then react with H⁺ to form H₂. TEOA plays a role as a hole scavenger for the reaction.

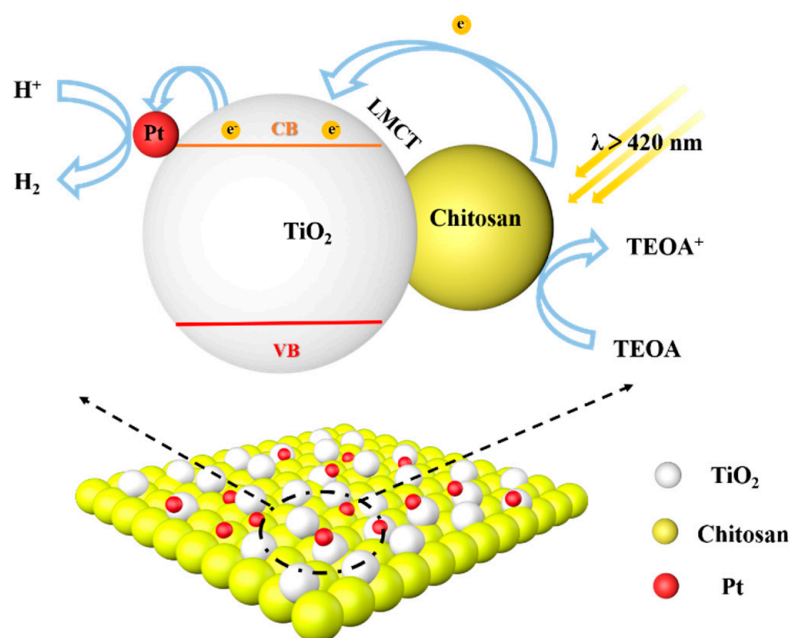


Figure 7. A schematic illustration of the photocatalytic mechanism for H₂ production through water reduction over a Pt-chitosan-TiO₂ charge transfer complex.

3. Materials and Methods

3.1. Materials

Chitin, N,N-dimethylformamide, hydrochloric acid (HCl), and chloroplatinic acid hexahydrate ($\text{H}_2\text{PtCl}_6 \cdot 6\text{H}_2\text{O}$) were purchased from Aladdin (Shanghai, China). Methyl orange (MO), sodium hydroxide (NaOH), and sodium borohydride (NaBH_4) were provided by Sinopharm (Shanghai, China). Triethanolamine (TEOA) was purchased from Tianjin Fuchen Chemical Reagent Factory (Tianjin, China). Titanium tetraisopropoxide ($\text{C}_{12}\text{H}_{28}\text{O}_4\text{Ti}$) was provided by Sigma-Aldrich (Shanghai, China). All solutions were prepared using deionized (DI) water.

3.2. Preparation of Photocatalysts

Chitosan with different degrees of deacetylation was prepared by a concentrated alkali method [39]. We uniformly dispersed 1 g chitin in 25 mL of 50% NaOH solution. After that, the solution was stirred at 90 °C for a fixed length of time. The reacted mixtures were washed with deionized water for eliminating the excess lye until the pH of the solution was neutral. The obtained products were then placed in an oven at 80 °C and dried for 8 h. Finally, different deacetylation degrees of chitosan samples were obtained and denoted as DDn, where *n* reflects the degree of deacetylation of chitosan.

Chitosan-TiO₂ complexes were synthesized by a sol-gel method. Titanium sol was formed by hydrolyzing titanium tetraisopropoxy under acidic conditions and dialyzing the suspension to pH~4 [40]. Calcination of 100 mL of TiO₂ sol yielded 3 g of powder. To obtain mDDn-TiO₂ (where *m* = 5%, 10%, or 20%), DDn (0.0355, 0.075, and 0.169 g) was dispersed in 25 mL of titanium sol and 10 mL of deionized water and then mechanically stirred at ambient temperature. After being dried in a microwave, the gels were calcined at different temperatures (150, 200, or 250 °C) in a muffle furnace and maintained for 3 h. Finally, samples of mDDn-Tt were obtained, where *m* is the content of chitosan, *T* is the TiO₂, and *t* is the calcination temperature.

Pt-mDDn-Tt samples were synthesized by an impregnation method. We dispersed 1 g of DDn-TiO₂ in 1.34 mL of chloroplatinic acid hexahydrate ($\text{H}_2\text{PtCl}_6 \cdot 6\text{H}_2\text{O}$; 10 mg·mL⁻¹) by sonication for 30 s. Then, 2 mL of mixed aqueous solution containing 0.1 mol·mL⁻¹ of sodium borohydride (NaBH_4) and 0.1 mol·mL⁻¹ of sodium hydroxide (NaOH) was added. After that, the mixture was sonicated for 30 s. The mixture was then filtered, washed, dried, and ground to obtain the Pt-mDDn-Tt photocatalyst.

3.3. Determination of Degree of Deacetylation

The degree of deacetylation of chitosan was evaluated via an acid-base titration. Chitosan (0.25 g) was dissolved in 20 mL 0.1 M of HCl at 25 °C, and then two drops of MO indicator were added. 0.1 M of NaOH was used to titrate the solution until the color of the solution changed to orange-yellow. The degree of deacetylation of chitosan was calculated using:

$$\text{NH}_2\% = [(\text{C}_1\text{V}_1 - \text{C}_2\text{V}_2) \times 0.016] / [\text{G} (100 - \text{W})] \times 100$$

$$\text{DD}\% = \text{NH}_2\% / 9.94\% \times 100\%$$

where *C*₁ is the concentration of HCl (M); *C*₂ is the concentration of NaOH (M); *V*₁ is the volume of HCl added (mL); *V*₂ is the volume of NaOH added by titration (mL); *G* is the sample weight (g); and *W* is the sample water content (%), 0.016, equal to NH₂ content (g) in 1 mL of 1 M HCl, 9.94%: chitosan theoretical NH₂ content.

3.4. Characterization

Thermogravimetric analysis (TGA) was recorded on a Netzsch Sta 449C (Netzsch, Selb, Germany) thermal analysis instrument. The X-ray diffraction (XRD) patterns of samples were performed on a Bruker D8 Advance X-ray diffractometer (D8 Advanve, Bruker, Ettlingen, Germany) with Cu-K α radiation, running at an accelerating voltage

of 40 kV and applied current of 40 mA. BaSO₄ was employed as a reference to record UV–visible diffuse reflectance spectra (DRS) on a Varian Cary 500 apparatus (Varian, Palo Alto, CA, USA) equipped with an integrating sphere. The FT-IR spectra of samples were studied using a Nicolet Nexus 670 FT-IR spectrometer (ThermoScientific, Waltham, MA, USA). BELSORP-mini II equipment (MicrotracBEL, Osaka, Japan) was used to study the N₂ adsorption-desorption isotherms and BJH pore size distribution of samples. The morphology of the as-prepared samples was captured by field-emission scanning electron microscopy (FESEM, JEOL JSM-7500F, JEOL, Tokyo, Japan), operated at 5 kV and 10 μA. TEM, high-resolution transmission electron microscopy (HRTEM), and elemental mapping images were filmed by a JEOL model JEM 2100 F instrument (JEOL, Tokyo, Japan) at an accelerating voltage of 200 kV. A monochromatic Al-Kα source was employed to perform the X-ray photoelectron spectroscopy (XPS) of the samples on a PHI Quantum 2000 system. Photoluminescence (PL) measurements were analyzed on a FLSP920 (EI) fluorescence spectrophotometer (Edinburgh Instruments, Livingston, UK). A 20 mg sample was used for tableting, and the excitation spectra were measured with an emission wavelength at 350 nm.

3.5. Photocatalytic Measurements

The photocatalytic H₂ evolution was carried out in a glass-closed photocatalytic activity evaluation system (Labsolar-6A, Perfectlight). A 300 W Xe lamp (PLS-SXE300/300UV, Perfectlight, Beijing, China) was used as the light source ($\lambda \geq 420$ nm). We dispersed 100 mg of as-synthesized sample in 100 mL of 10 vol% aqueous triethanolamine (TEOA) solution in a quartz reactor at a constant temperature of 5 °C. Before the irradiation, the evaluation system was degassed. The amount of H₂ produced from the water reduction was analyzed by a gas chromatograph (GC 9790, FuLi, China) equipped with a TCD detector.

3.6. Photoelectrochemical Measurements

The powder sample was prepared on fluorine-doped tin oxide (FTO) glass. We sonicated 5 mg of the sample in 0.5 mL of N,N-dimethylformamide to disperse it evenly. After that, the paste was spread onto the conductive surface of the FTO glass and then dried. All the photoelectrochemical measurements were tested in a three-electrode cell with a Pt plate and Ag/AgCl electrodes as the counter and reference electrodes, and the sample electrode as the working electrode. The electrochemical impedance spectroscopy (EIS) measurement and transient photocurrent were performed using an electrochemical workstation (Versa STAT3, Princeton Instruments, Acton, MA, USA) with 0.1 M KCl and 0.1 M Na₂SO₄ as the electrolyte. A 300 W Xe lamp (PLS-SXE300/300UV, Perfectlight) and UV cutoff filter ($\lambda > 420$ nm) were used as the radiation source.

4. Conclusions

In summary, a new Pt-chitosan-TiO₂ CT complex was synthesized via a sol-gel and impregnation method. The optical absorbance range of TiO₂ was expanded to the visible region, attributed to the LMCT mechanism that allows photo-excited electrons from the HOMO of chitosan to transfer to the conduction band of the TiO₂. By optimizing the preparation conditions of the photocatalysts (the degree of deacetylation of chitosan, additional amounts of chitosan and calcination temperature), the synthesized Pt-10%DD75-T200 showed outstanding photocatalytic activity (280.4 μmol) for H₂ evolution from water reduction after 3 h of visible-light irradiation. The underlying reaction mechanism for water reduction over a Pt-chitosan-TiO₂ CT complex under visible-light irradiation was proposed. This work provides a new idea for converting natural polysaccharide biomass waste into attractive functional materials, showing potential applications in visible-light-driven H₂ evolution from water reduction.

Supplementary Materials: The following supporting information can be downloaded at: <https://www.mdpi.com/article/10.3390/molecules27154673/s1>, Figure S1: UV-vis diffuse reflectance spectra of as-prepare Pt-Chitosan-TiO₂ samples; Figure S2: Control experiments for photocatalytic H₂ evolution reaction over Pt-10%DD75-T200; Figure S3: Action spectra of Pt-10%DD75-T200 (illumination time: 1 h, 10 vol% TEOA, pH = 11.3, 278 K); Figure S4: FT-IR spectra of Pt-10%DD75-T200 before and after irradiation; Figure S5: XPS spectra of Pt-10%DD75-T200 before and after irradiation; Figure S6: Excitation spectra of Pt-T200, Pt-10%DD45-T200 and Pt-10%DD75-T200; Table S1: UV-vis diffuse reflectance spectra of (a) DD45, DD75 and (c) as-prepare Pt-Chitosan-TiO₂ samples.

Author Contributions: Conceptualization, Y.L. (Yanru Liu), J.M. and Y.H.; data curation, Y.L. (Yanru Liu), J.M. and S.Y.; formal analysis, Y.L. (Yanru Liu) and J.M.; funding acquisition, Q.Q., S.Y. and H.X.; investigation, Y.L. (Yanru Liu) and J.M.; methodology, Y.L. (Yanru Liu), J.M. and H.X.; supervision, Y.L. (Yongjin Luo), Q.Q. and H.X.; visualization, Y.L. (Yanru Liu) and J.M.; writing—original draft, Y.L. (Yanru Liu) and J.M.; writing—review and editing, Y.L. (Yanru Liu), J.M., Y.H., Y.L. (Yongjin Luo), H.X., Q.Q. and S.Y. All authors have read and agreed to the published version of the manuscript.

Funding: This work was supported financially by the National Natural Science Foundation of China (NSFC 21875037 and 51502036) and the National Key Research and Development Program of China (2016YFB0302303 and 2019YFC1908203).

Institutional Review Board Statement: Not applicable.

Informed Consent Statement: Not applicable.

Data Availability Statement: The data presented in this study are available upon request from the corresponding author.

Acknowledgments: The authors of this study gratefully acknowledge Fujian Key Laboratory of Pollution Control (Fuzhou, China) for providing the facility for sample characterizations.

Conflicts of Interest: The authors declare no conflict of interest. The funders had no role in: the design of the study; in the collection, analyses, or interpretation of data; in the writing of the manuscript; or in the decision to publish the results.

Sample Availability: Samples of the compounds are not available from the authors.

References

1. Liu, J.; Ma, N.; Wu, W.; He, Q. Recent progress on photocatalytic heterostructures with full solar spectral responses. *Chem. Eng. J.* **2020**, *393*, 124719. [[CrossRef](#)]
2. Niu, J.N.; Albero, J.; Atienzar, P.; Garcia, H. Porous single-crystal-based inorganic semiconductor photocatalysts for energy production and environmental remediation: Preparation, modification, and applications. *Adv. Funct. Mater.* **2020**, *30*, 1908984. [[CrossRef](#)]
3. Mao, J.; Zhong, H.; Liu, X.; Qian, Q.; Luo, Y.; Xiao, L.; Xue, H. Electrospinning preparation of GaN:ZnO solid solution nanorods with visible-light-driven photocatalytic activity toward H₂ production. *Appl. Sci.* **2021**, *11*, 10854. [[CrossRef](#)]
4. Shukla, B.K.; Rawat, S.; Gautam, M.K.; Bhandari, H.; Garg, S.; Singh, J. Photocatalytic degradation of orange G dye by using bismuth molybdate: Photocatalysis optimization and modeling via definitive screening designs. *Molecules* **2022**, *27*, 2309. [[CrossRef](#)]
5. Jia, Y.; Liu, P.B.; Wang, Q.Y.; Wu, Y.; Cao, D.D.; Qiao, Q.A. Construction of Bi₂S₃-BiOBr nanosheets on TiO₂ NTA as the effective photocatalysts: Pollutant removal, photoelectric conversion and hydrogen generation. *J. Colloid Interface Sci.* **2021**, *585*, 459–469. [[CrossRef](#)] [[PubMed](#)]
6. Hunge, Y.; Yadav, A.; Dhodamani, A.; Suzuki, N.; Terashima, C.; Fujishima, A.; Mathe, V. Enhanced photocatalytic performance of ultrasound treated GO/TiO₂ composite for photocatalytic degradation of salicylic acid under sunlight illumination. *Ultrason. Sonochem.* **2019**, *61*, 104849. [[CrossRef](#)]
7. Liu, Y.L.; Wu, S.S.; Liu, J.; Xie, S.B.; Liu, Y.J. Synthesis of g-C₃N₄/TiO₂ nanostructures for enhanced photocatalytic reduction of U(VI) in water. *RSC Adv.* **2021**, *11*, 4810–4817. [[CrossRef](#)]
8. Djellabi, R.; Yang, B.; Wang, Y.; Cui, X.; Zhao, X. Carbonaceous biomass-titania composites with Ti-O-C bonding bridge for efficient photocatalytic reduction of Cr(VI) under narrow visible light. *Chem. Eng. J.* **2019**, *366*, 172–180. [[CrossRef](#)]
9. Li, Z.; Wang, S.; Wu, J.; Zhou, W. Recent progress in defective TiO₂ photocatalysts for energy and environmental applications. *Renew. Sustain. Energy Rev.* **2021**, *156*, 111980. [[CrossRef](#)]
10. Diaz-Angulo, J.; Lara-Ramos, J.; Mueses, M.; Hernández-Ramírez, A.; Puma, G.L.; Machuca-Martínez, F. Enhancement of the oxidative removal of diclofenac and of the TiO₂ rate of photon absorption in dye-sensitized solar pilot scale CPC photocatalytic reactors. *Chem. Eng. J.* **2019**, *381*, 122520. [[CrossRef](#)]

11. Yang, L.; Bai, X.; Shi, J.; Du, X.; Xu, L.; Jin, P. Quasi-full-visible-light absorption by D35-TiO₂/g-C₃N₄ for synergistic persulfate activation towards efficient photodegradation of micropollutants. *Appl. Catal. B-Environ.* **2019**, *256*, 117759. [[CrossRef](#)]
12. Qing, X.; Yuan, L.; Wang, C.; Bi, M.; Wang, Y.; Weng, X. Structural and visible-near infrared optical properties of (Fe, Mo)-co-doped TiO₂ for colored cool pigments. *J. Alloys Compd.* **2020**, *826*, 153946. [[CrossRef](#)]
13. Park, B.G. Photocatalytic activity of TiO₂-doped Fe, Ag, and Ni with N under visible light irradiation. *Gels* **2022**, *8*, 14. [[CrossRef](#)] [[PubMed](#)]
14. Han, Q.; Wu, C.; Jiao, H.; Xu, R.; Wang, Y.; Xie, J.; Guo, Q.; Tang, J. Rational design of high-concentration Ti³⁺ in porous carbon-doped TiO₂ nanosheets for efficient photocatalytic ammonia synthesis. *Adv. Mater.* **2021**, *33*, 2008180. [[CrossRef](#)]
15. Ma, Z.L.; Shi, L.Y.; Qu, W.W.; Hu, Q.; Chen, R.F.; Wang, Y.J.; Chen, Z. Microwave-assisted synthesis of an RGO/CdS/TiO₂ step-scheme with exposed TiO₂ {001} facets and enhanced visible photocatalytic activity. *RSC Adv.* **2020**, *10*, 43447–43458. [[CrossRef](#)]
16. Wang, C.J.; Zhao, Y.L.; Xu, H.; Li, Y.F.; Wei, Y.C.; Liu, J.; Zhao, Z. Efficient Z-scheme photocatalysts of ultrathin g-C₃N₄-wrapped Au/TiO₂-nanocrystals for enhanced visible-light-driven conversion of CO₂ with H₂O. *Appl. Catal. B-Environ.* **2020**, *263*, 118314. [[CrossRef](#)]
17. Wang, Y.T.; Zhu, C.Z.; Zuo, G.C.; Guo, Y.; Xiao, W.; Dai, Y.X.; Kong, J.J.; Xu, X.M.; Zhou, Y.X.; Xie, A.M.; et al. 0D/2D Co₃O₄/TiO₂ Z-scheme heterojunction for boosted photocatalytic degradation and mechanism investigation. *Appl. Catal. B-Environ.* **2020**, *278*, 119298. [[CrossRef](#)]
18. Zhang, L.; Yang, J.; Zhao, X.Y.; Xiao, X.; Sun, F.Q.; Zuo, X.X.; Nan, J.M. Small-molecule surface-modified bismuth-based semiconductors as a new class of visible-light-driven photocatalytic materials: Structure-dependent photocatalytic properties and photosensitization mechanism. *Chem. Eng. J.* **2020**, *380*, 122546. [[CrossRef](#)]
19. Zhang, G.; Kim, G.; Choi, W. Visible light driven photocatalysis mediated via ligand-to-metal charge transfer (LMCT): An alternative approach to solar activation of titania. *Energy Environ. Sci.* **2014**, *7*, 954–966. [[CrossRef](#)]
20. Zhang, L.; Wu, B.; Zhang, G.; Gan, Y.; Zhang, S. Enhanced decomplexation of Cu(II)-EDTA: The role of acetylacetone in Cu-mediated photo-fenton reactions. *Chem. Eng. J.* **2019**, *358*, 1218–1226. [[CrossRef](#)]
21. Choudhury, B.; Bayan, S.; Choudhury, A.; Chakraborty, P. Narrowing of band gap and effective charge carrier separation in oxygen deficient TiO₂ nanotubes with improved visible light photocatalytic activity. *J. Colloid Interface Sci.* **2016**, *465*, 1–10. [[CrossRef](#)] [[PubMed](#)]
22. Karthik, P.; Vinoth, R.; Selvam, P.; Balaraman, E.; Navaneethan, M.; Hayakawa, Y.; Neppolian, B. A visible-light active catechol-metal oxide carbonaceous polymeric material for enhanced photocatalytic activity. *J. Mater. Chem. A* **2017**, *5*, 384–396. [[CrossRef](#)]
23. Kim, S.; Moon, G.-H.; Kim, G.; Kang, U.; Park, H.; Choi, W. TiO₂ complexed with dopamine-derived polymers and the visible light photocatalytic activities for water pollutants. *J. Catal.* **2017**, *346*, 92–100. [[CrossRef](#)]
24. Karthik, P.; Neppolian, B. TiO₂-glucose LMCT complex/reduced graphene oxide sheet (rGO): An efficient visible light photocatalyst for Cr(VI) reduction. *J. Environ. Chem. Eng.* **2018**, *6*, 3664–3672. [[CrossRef](#)]
25. Kim, G.; Choi, W. Charge-transfer surface complex of EDTA-TiO₂ and its effect on photocatalysis under visible light. *Appl. Catal. B-Environ.* **2010**, *100*, 77–83. [[CrossRef](#)]
26. Kim, G.; Lee, S.-H.; Choi, W. Glucose-TiO₂ charge transfer complex-mediated photocatalysis under visible light. *Appl. Catal. B-Environ.* **2015**, *162*, 463–469. [[CrossRef](#)]
27. Li, Y.; Zhang, J.; Zhan, C.; Kong, F.; Li, W.; Yang, C.; Hsiao, B.S. Facile synthesis of TiO₂/CNC nanocomposites for enhanced Cr(VI) photoreduction: Synergistic roles of cellulose nanocrystals. *Carbohydr. Polym.* **2020**, *233*, 115838. [[CrossRef](#)]
28. Arasukumar, B.; Prabakaran, G.; Gunalan, B.; Moovendhan, M. Chemical composition, structural features, surface morphology and bioactivities of chitosan derivatives from lobster (*Thenus unimaculatus*) shells. *Int. J. Biol. Macromol.* **2019**, *135*, 1237–1245. [[CrossRef](#)]
29. Sugashini, S.; Gomathi, T.; Devi, R.A.; Sudha, P.N.; Rambabu, K.; Banat, F. Nanochitosan/carboxymethyl cellulose/TiO₂ biocomposite for visible-light-induced photocatalytic degradation of crystal violet dye. *Environ. Res.* **2022**, *204*, 112047. [[CrossRef](#)]
30. Li, Q.-H.; Dong, M.; Li, R.; Cui, Y.-Q.; Xie, G.-X.; Wang, X.-X.; Long, Y.-Z. Enhancement of Cr(VI) removal efficiency via adsorption/photocatalysis synergy using electrospun chitosan/g-C₃N₄/TiO₂ nanofibers. *Carbohydr. Polym.* **2021**, *253*, 117200. [[CrossRef](#)]
31. Balakrishnan, A.; Appunni, S.; Gopalram, K. Immobilized TiO₂/chitosan beads for photocatalytic degradation of 2,4-dichlorophenoxyacetic acid. *Int. J. Biol. Macromol.* **2020**, *161*, 282–291. [[CrossRef](#)] [[PubMed](#)]
32. Chen, C.-H.; Wang, F.-Y.; Mao, C.-F.; Liao, W.-T.; Hsieh, C.-D. Studies of chitosan: II. Preparation and characterization of chitosan/poly(vinyl alcohol)/gelatin ternary blend films. *Int. J. Biol. Macromol.* **2008**, *43*, 37–42. [[CrossRef](#)] [[PubMed](#)]
33. Liu, Z.; Ge, X.; Lu, Y.; Dong, S.; Zhao, Y.; Zeng, M. Effects of chitosan molecular weight and degree of deacetylation on the properties of gelatine-based films. *Food Hydrocolloid.* **2012**, *26*, 311–317. [[CrossRef](#)]
34. Xue, H.; Chen, Y.; Liu, X.; Qian, Q.; Luo, Y.; Cui, M.; Chen, Y.; Yang, D.-P.; Chen, Q. Visible light-assisted efficient degradation of dye pollutants with biomass-supported TiO₂ hybrids. *Mater. Sci. Eng. C* **2018**, *82*, 197–203. [[CrossRef](#)]
35. Liang, H.; Lv, C.; Chen, H.; Wu, L.; Hou, X. Facile synthesis of chitosan membranes for visible-light-driven photocatalytic degradation of tetracycline hydrochloride. *RSC Adv.* **2020**, *10*, 45171–45179. [[CrossRef](#)] [[PubMed](#)]
36. Kang, J.; Liu, H.; Zheng, Y.-M.; Qu, J.; Chen, J.P. Systematic study of synergistic and antagonistic effects on adsorption of tetracycline and copper onto a chitosan. *J. Colloid Interface Sci.* **2010**, *344*, 117–125. [[CrossRef](#)] [[PubMed](#)]

37. Liu, Y.; Liu, X.; Lu, D.; Fang, P.; Xiong, R.; Wei, J.; Pan, C. Carbon deposited TiO₂-based nanosheets with enhanced adsorption ability and visible light photocatalytic activity. *J. Mol. Catal. A-Chem.* **2014**, *392*, 208–215. [[CrossRef](#)]
38. Vovk, E.I.; Kalinkin, A.V.; Smirnov, M.Y.; Klembovskii, I.O.; Bukhtiyarov, V.I. XPS study of stability and reactivity of oxidized Pt nanoparticles supported on TiO₂. *Phys. Chem. C* **2017**, *121*, 17297–17304. [[CrossRef](#)]
39. Nwe, N.; Furuike, T.; Tamura, H. Isolation and characterization of chitin and chitosan from marine origin. *Adv. Food Nutr. Res.* **2014**, *72*, 1–15.
40. Wang, J.; Qian, Q.; Chen, Q.; Liu, X.-P.; Luo, Y.; Xue, H.; Li, Z. Significant role of carbonate radicals in tetracycline hydrochloride degradation based on solar light-driven TiO₂-seashell composites: Removal and transformation pathways. *Chin. J. Catal.* **2020**, *41*, 1511–1521. [[CrossRef](#)]